

A New Healing Strategy for Metals: Programmed Damage and Repair

Mariia Arsenko¹, Florent Hannard¹, Lipeng Ding^{1,2,3}, Lv Zhao^{1,4}, Eric Maire⁵,
Julie Villanova⁶, Hosni Idrissi^{1,2}, Aude Simar^{1,*}

¹ Institute of Mechanics, Materials and Civil Engineering, UCLouvain, Louvain-la-Neuve 1348, Belgium

² Electron Microscopy for Materials Science, University of Antwerp, Antwerp 2000, Belgium

³ Key laboratory for Light-weight Materials, Nanjing Tech University, Nanjing 211816, China

⁴ Department of Mechanics, School of Aerospace Engineering, Huazhong University of Science and Technology, Wuhan 430074, China

⁵ Mateis, INSA Lyon, Université de Lyon, Villeurbanne F-69621, France

⁶ ESRF - The European Synchrotron, Grenoble 38043, France

**corresponding authors*, E-mail: aude.simar@uclouvain.be

Keywords: Self-healing, Aluminum alloys, Synchrotron radiation computed tomography, In situ TEM, In situ tension test

Abstract

Self-healing strategies aim at avoiding part repair or even replacement, which is time consuming, expensive and generates waste. However, strategies for metallic systems are still under-developed and solid-state solutions for room temperature service are limited to nano-scale damage repair. Here we propose a new healing strategy of micron-sized damage requiring only short and low temperature heating. This new strategy is based on damage localization particles, which can be healed by fast diffusing atoms of the matrix activated during heat treatment. The healing concept was successfully validated with a commercial aluminum alloy and manufactured by Friction Stir Processing (FSP). Damage was demonstrated to initiate on particles that were added to the matrix during material processing. In situ 2D and 3D nano-imaging confirmed healing of the damaged material and showed that heating this material for 10 min at 400 °C is sufficient to heal incipient damage with complete filling of 70% of all damage (and up to 90% when their initial size is below 0.2 μm). Furthermore, strength is

34 retained and the work of fracture of the alloy is improved by about 40% after healing. The
35 proposed Programmed Damage and Repair healing strategy could be extended to other metal
36 based systems presenting precipitation.

37

38 **1. Introduction**

39

40 Aluminum alloys have many applications in aerospace or transportation industry, where
41 the strength-to-weight ratio should be maximized [1–3]. However, the relatively low damage
42 tolerance of high strength Al alloys remains a major challenge for increasing product lifetime
43 [3,4]. During service, parts might accumulate damage requiring repair or even replacement,
44 which is time consuming, expensive and generates waste. Now, aluminum alloys are facing one
45 limitation intrinsic to metallic materials: once damage has initiated, it will not vanish [5]!

46 Self-healing (SH) materials are able to suppress initiated damage [5–9]. This strategy
47 brings about a new paradigm in materials design and is already well-developed for polymers,
48 cement, asphalt, and ceramics, but under-exploited for metallic materials [5,6,9]. The general
49 difficulty with SH metallic systems is the low mobility of atoms at room temperature and often
50 the need for an external driving force to promote mass transfer, without sacrificing the strength
51 of the system [5–10].

52 Several strategies are currently under development for SH metal-based systems which
53 were categorized by Grabowski and Tazan depending on the dimension of the healed damage
54 [6]. Strategies in systems where millimeter-scale cracks can be healed are based on electro-
55 healing (e.g. for steels and Ti alloys) [11,12] or liquid-based systems based on melting of one
56 component of the system (e.g. low melting point Sn-Bi phase) filling the cracks [5–8,13]. Both
57 systems correspond to a group of assisted healing, where the electro-healing group needs
58 external electrical field and the other one needs external heat [5].

59 Electro-healing is a recently developed and promising strategy for steels, Ni and Ti
60 alloys, that can be divided into two groups: electro-healing inside electrolyte solution and
61 electropulsing treatment without electrolyte solution [14]. One advantage of these strategies is
62 that they do not require any alloy microstructural modifications. However, the use of electrolyte
63 solution is a practical limitation and no results are available for Al alloys. More details on these
64 healing strategies can be found elsewhere [5,6,14].

65 Liquid-based systems can be divided into three groups: the ones using solder tubes or
66 capsules containing healing agent, the ones using coating as a healing agent and the ones using
67 low melting point eutectics (also exploiting shape memory alloys) [14]. However, their

68 applicability is limited by the requirement to maintain the shape of the part, prevent liquid
69 leakage and solidification cracking during the healing cycle [5,7]. Furthermore, these materials
70 have limited potential for structural components due to their low mechanical properties and
71 their high anisotropy [5,6].

72 Another SH strategy in metals is based on the solid-state diffusion of a healing agent
73 leading to precipitation inside nano- and micro-scale voids of a new phase [5,6,15]. This healing
74 strategy requires the availability of atoms in solid-solution in supersaturated state and their
75 mobility and is thus only applicable for selected alloys. Common systems here are precipitation
76 hardenable Al alloys in underaged state where alloying elements are in super-saturated solid
77 solution offering healing potential as presented in Ref. [16,17]. Underaged Al alloys are in low
78 strength state, presenting less interest for applications requiring high strength. Current solid-
79 state precipitation-based healing metals can be divided into two categories depending on
80 external trigger used to promote diffusion: Thermally activated Diffusion and Precipitation
81 (TDP) and Pipe Diffusion and Precipitation (PDP), see Figure 1a.

82 Thermally activated Diffusion and Precipitation TDP (Figure 1a,b) is facilitated by (i)
83 nanoscale cavities formed at grain boundaries, (ii) relatively high homologous temperatures
84 (Figure 1b) and (iii) relatively long service time, all typical of creep damage [15,18]. One major
85 difficulty associated with TDP is that the healing precipitation happens not only at the damaged
86 area but also throughout the microstructure, reducing the number of super-saturated solute
87 atoms available in the matrix for healing [6,18].

88 Pipe Diffusion and Precipitation PDP (Figure 1a,b) falls within the low-temperature
89 applicability window where diffusion is very slow for transport of solute elements to damage
90 sites. This is typical of long fatigue loadings during which microplasticity generates regions of
91 vacancies and high dislocation densities where damage is more likely to nucleate due to
92 dislocation pile-ups [6]. Precipitation takes place in these regions due to pipe diffusion, i.e.
93 diffusion of solute elements along dislocations. PDP demonstrated improved fatigue resistance
94 in commercial Al-Cu-Mg alloys in underaged state compared to peak-aged state [17,19].
95 Limitations of PDP are (i) the capacity to only heal nanoscale damage (Figure 1c) and (ii)
96 environmental effects to the near-surface cracks hindering crack healing [5,6,20].

97

98

99

100

101

102 **2. A new healing strategy: Programmed Damage and Repair**

103

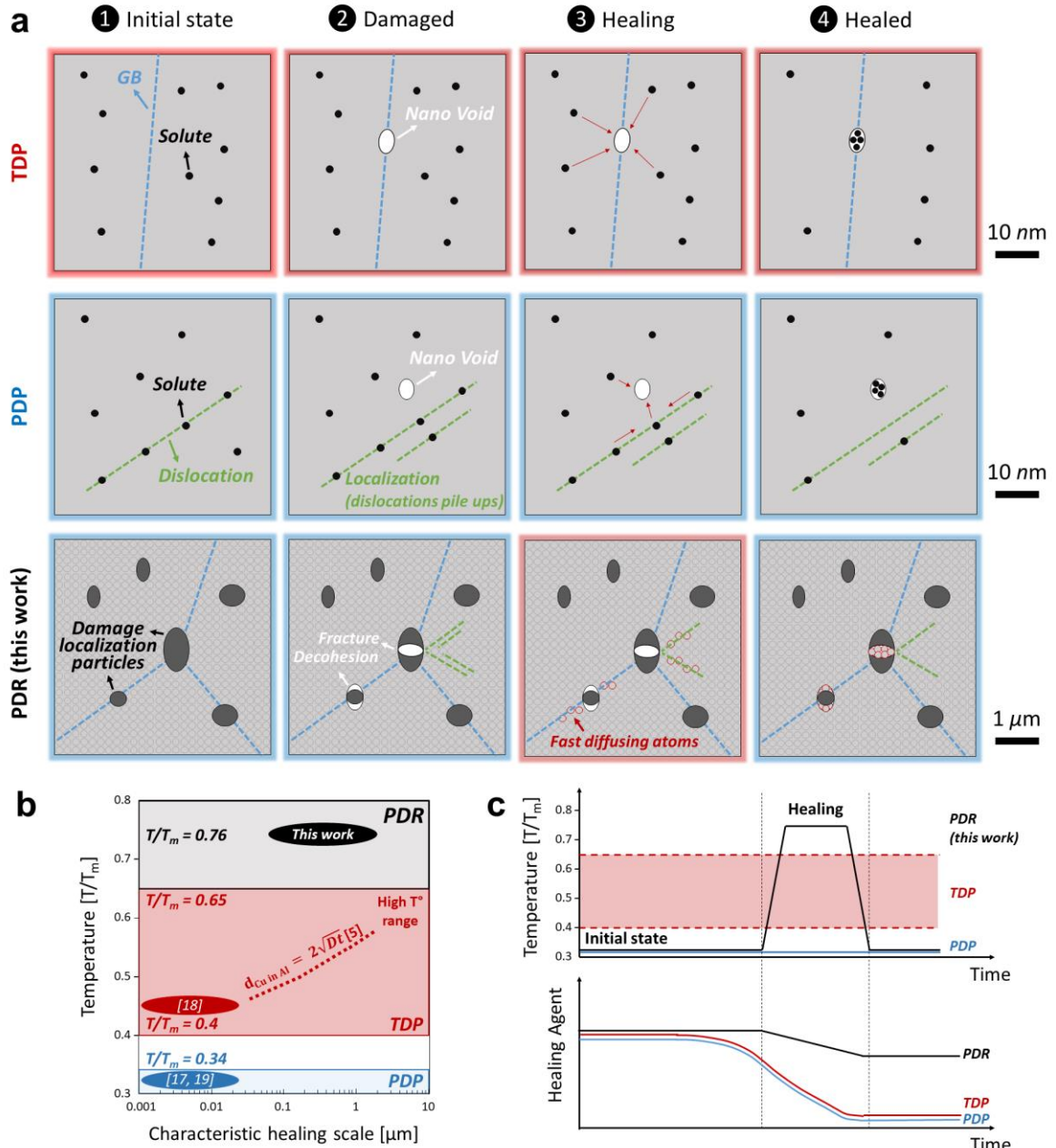
104 Here, we propose a new solid-state healing strategy called *Programmed Damage and*
105 *Repair* (PDR, Figure 1a, bottom) applied to an Al alloy. It incorporates damage localization
106 particles within a commercial Al alloy. Damage primarily nucleates on these particles (hence
107 *Programmed Damage*) modifying the common void nucleation mechanism in Al alloys, i.e. by
108 fracture or decohesion of iron-rich intermetallics [21,22]. During service, loading is interrupted
109 and a healing heat treatment (HHT) triggers diffusion to heal these voids (hence *Repair*).
110 Temperature and time are selected to minimize microstructural changes that would lead to
111 strength decrease, keeping a reasonable healing efficiency.

112 Our new PDR strategy presents a notable difference to the two strategies discussed
113 above. While the TDP and PDP (Figure 1a) concepts use precipitation event at nano-voids as
114 healing mechanism, the PDR strategy is based on fully precipitated microstructure where these
115 precipitates play the role of “damage localization particles”. The second difference relates to
116 the healing mechanism. In our new concept, the matrix itself is the healing source, not for
117 precipitation as our microstructure is already fully precipitated, but for matrix penetration into
118 the crack by exploiting fast atomic diffusion mechanisms.

119 This PDR strategy presents several advantages compared to TDP and PDP. In particular,
120 although PDR requires thermal activation like TDP, the material is heated for only a limited
121 time (Figure 1c, top) at temperatures slightly above the upper limit of TDP strategy to ensure
122 sufficient diffusion. Furthermore, PDR is not restricted to healing nanoscale damage contrary
123 to PDP (Figure 1b), i.e. PDR repairs damage at a scale controlled by the damage localization
124 particles. Moreover, in the TDP and PDP strategies, precipitation is difficult to control and leads
125 to a reduction in healing efficiency [6,18]. The PDR strategy relies on strengthening and
126 particles that strengthen the alloy and also serve as well-controlled damage sites and healing
127 agent concentrators. The healing efficiency is thus expected to be maintained for multiple
128 healing cycles (Figure 1c, bottom).

129 In addition, healing potential can be enhanced by a high density of crystallographic
130 defects such as vacancies, dislocations, subgrain and grain boundaries and eventually internal
131 surfaces (i.e. the surfaces of the induced voids). Such defects provide diffusion shortcuts and
132 thus increase diffusion rates. Processing methods that can achieve such microstructures can thus
133 enhance the material’s healing potential [23,24].

134



135

136

137

138

139

140

141

142

143

144

145

146

Figure 1. Healing strategies in metallic materials. (a) Schematic overview of solid-state self-healing strategies in metals inspired from Grabowski and Tasan [6] (TDP = Thermally activated Diffusion and Precipitation, PDP = Pipe Diffusion and Precipitation and PDR = Programmed Damage and Repair). (b) T/T_m – homologous temperature as a function of characteristic healing scale (temperature (in K), T_m – melting temperature (in K)). Temperatures below $T/T_m \approx 0.34$ (in blue) correspond to the PDP strategy operating at room temperature. The “High T° range” (in red) corresponds to TDP strategy and is inspired from [5]. The limits are defined as upper and lower operation limits for creep-loaded samples. The red dotted line corresponds to the calculated theoretical healable damage size evolution with temperature assuming a characteristic diffusion length of Cu in pure Al after 10^5 seconds. The PDR strategy points are placed at 400°C ($T/T_m \approx 0.76$), see section 4.3. Numbers [17,19] and [18] in the figure refer to the corresponding papers in the reference list. (c) Evolution of homologous temperature and healing agent concentration with time for these strategies.

147 **3. Experimental methods**

148

149 **3.1. Manufacturing**

150

151 To obtain the desired microstructure, Friction Stir Processing (FSP) was applied on
152 commercial Al 6063 alloy, a representative alloy of the Al-Mg-Si system. FSP is a well-known
153 technique for ductility and strength improvement of aluminum alloys as well as for particles
154 incorporation to obtain Aluminum based Matrix Composites (AMCs) [2,25,26]. FSP leads to
155 refinement and homogenization of the microstructure and the processed material typically
156 contains a high amount of crystal defects, i.e. vacancies, dislocations, subgrain and grain
157 boundaries. These microstructural features provide, on the one hand, nucleation sites for
158 precipitation and, on the other hand, increasing healing potential by the presence of diffusion
159 shortcuts for fast-diffusing atoms [14,24].

160 Friction Stir Processing (FSP) was applied on an Al6063-T4 plate (300x70x5 mm) (see
161 Supplementary material 1). To introduce the damage localization particles, a 240x5x0.5 mm³
162 groove was machined in the middle of the plate and filled with a 99.9% purity Mg strip of the
163 same geometry, covered by a 1 mm thick cold rolled 6063 plate. FSP was conducted on a FSW
164 machine E256 (TRA-C Industry), using a H13 steel tool. The FSP tool has a 20 mm diameter
165 shoulder, a 5.6 mm diameter and 2 mm long pin, penetrating 2.2 mm into the plate. Sixteen
166 passes of FSP were performed with a rotational speed of 1000 rpm and a traverse speed of 400
167 mm/min in order to ensure good distribution of Mg.

168

169 **3.2. Alloy composition and conventional microstructure observations**

170

171 Chemical analysis was conducted by Inductively Coupled Plasma (ICP) - Atomic
172 Emission Spectroscopy (AES) on a iCAP 6000 equipment (Thermo Scientific). Microstructural
173 characterization was performed using Scanning Electron Microscopy (SEM, Zeiss ultra 55).
174 Further investigations on damage localization particles, their chemical composition and the
175 composition of the matrix were performed with FEI Osiris Transmission Electron Microscope
176 (TEM) operated at 200kV and equipped with a CHEMISTEM detector. Samples were prepared
177 from the top surface of the nugget zone at a depth of at least 0.5 mm. TEM thin foils were
178 prepared by soft ion milling (Gatan Duo Mill 600 machine).

179

180

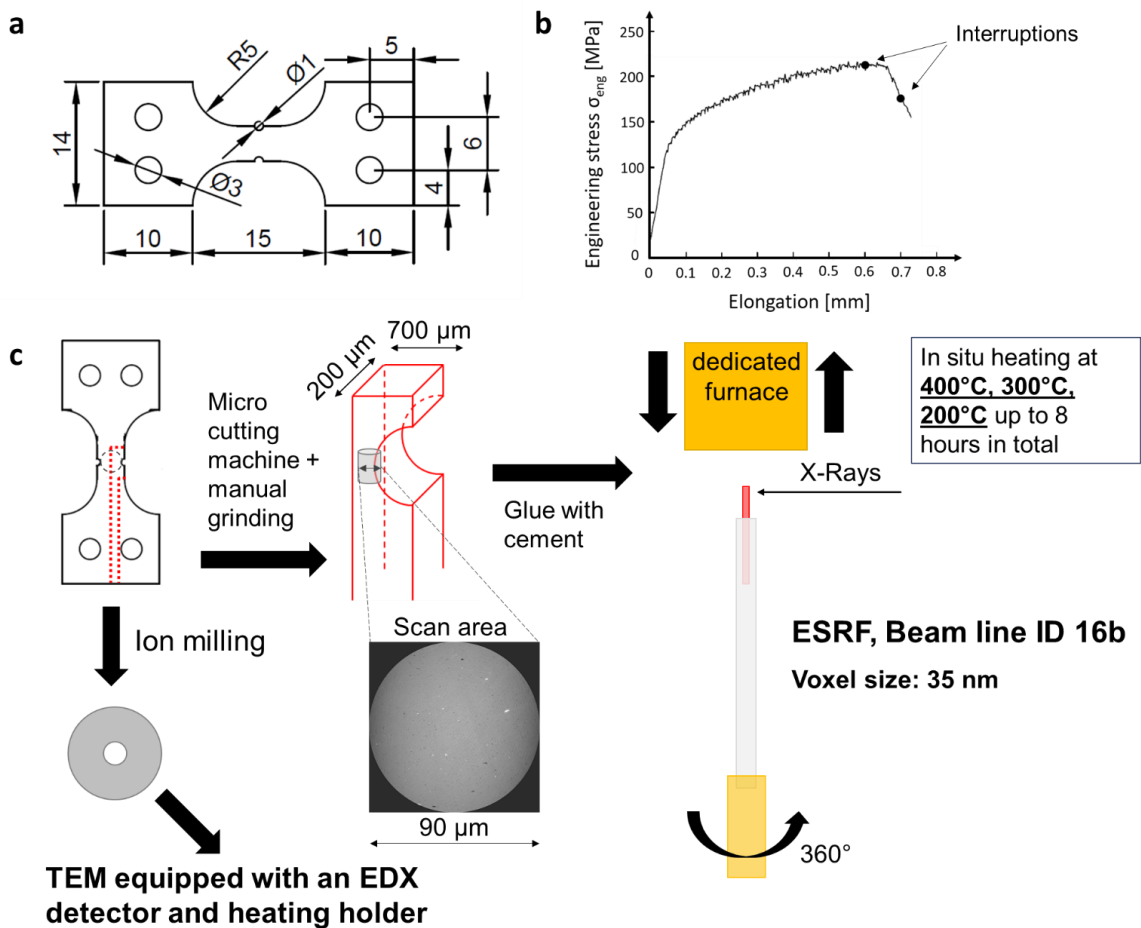
181 **3.3. In situ SEM tensile test**

182

183 To reveal damage mechanisms, in situ uniaxial tensile tests were performed inside the
 184 SEM using a micro-tensile machine (Gatan microtest tensile stage). Void formation and
 185 coalescence could thus be monitored. Flat samples with a thickness of 1 mm were extracted
 186 from the top part of the FSPed plate (see Supplementary material 1). The detailed geometry of
 187 these samples is provided in Figure 2a. The loading rate was set to 0.1 mm/min. To force the
 188 crack initiation site and facilitate observations, the flat tensile samples contained U-shaped
 189 notches on both sides (Figure 2a).

190

191



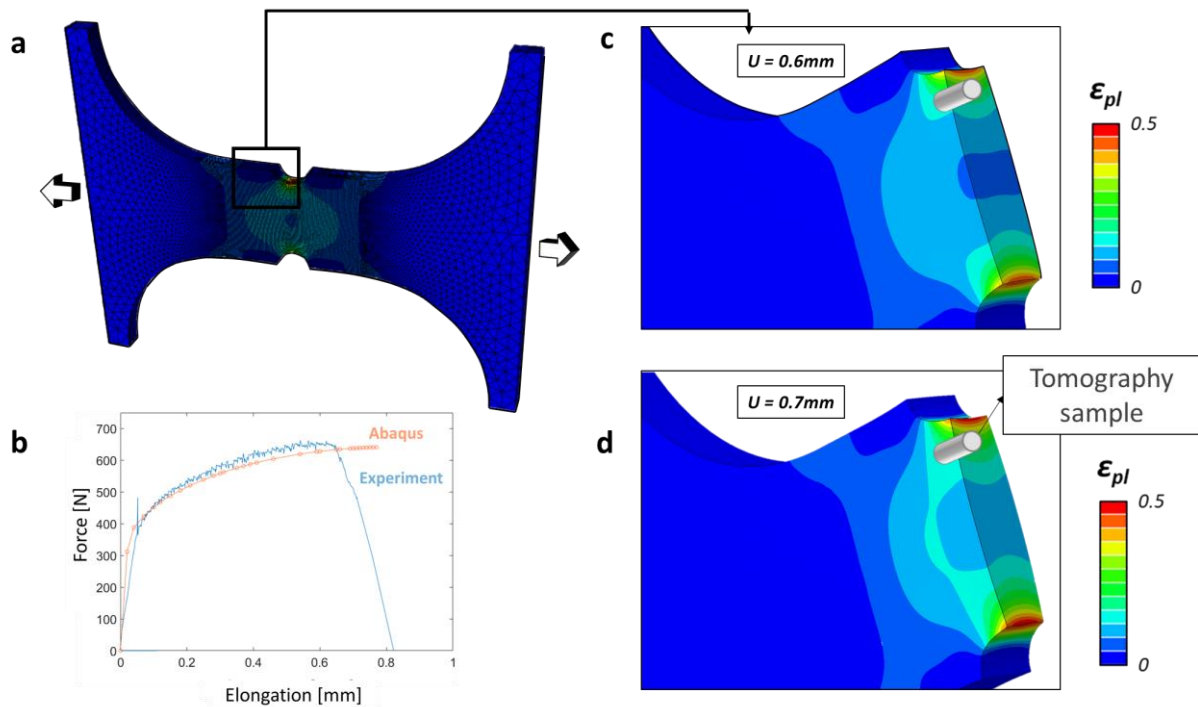
192

193 **Figure 2.** Samples preparation for in situ SEM tensile testing, in situ TEM heating and in situ 3D X-Ray nano-
 194 imaging. (a) Geometry of in situ SEM tensile test sample (thickness about 1 mm); (b) Representative interrupted
 195 engineering stress-strain curve at 0.6 or 0.7 mm elongation in comparison with a curve where the test was
 196 performed without observation and until fracture; (c) Steps of sample preparation and schematic for in situ 3D
 197 X-Ray nano-imaging and in situ TEM heating experiments.

198

199 These in-situ tensile tests have been interrupted at elongations of 0.6 mm or 0.7 mm.
200 These two levels of elongation have been selected in order to ensure a significant number of
201 voids nucleated from the reinforcement particles.

202 In order to estimate more precisely the applied strain in the sub-specimen (extracted for
203 in situ 3D X-Ray nano-imaging using holotomography) at the notch root (see Figure 2c), finite
204 element (FE) analysis of the SEM tensile tests was performed (see Figure 3). The input file of
205 this model was constructed and solved with the general-purpose software ABAQUS (version
206 2019). Young's modulus and hardening law were identified from the experimental macroscopic
207 stress-strain curves of uniaxial tensile tests (section 3.6). Isotropic hardening was assumed and
208 3D linear hexahedral elements (C3D8R) were used. The FE procedures are fully standard and
209 convergence of the results was carefully checked (with 16 elements in the thickness direction).
210



211
212 **Figure 3:** Finite element analysis of SEM tensile samples. (a) Finite element mesh of the whole specimen; (b)
213 Experimental and computed Force-displacement curves of the SEM tensile tests. Contour plots of von Mises
214 equivalent strain within a cross-section through the center of the notch for an elongation of (c) 0.6 and (d) 0.7
215 mm.

216
217 Figure 3 shows both the experimental and computed force-displacement curves of the
218 SEM tensile tests. A good agreement is observed up to elongation value of approximately 0.75
219 mm. Figure 3c-d shows contour plots of von Mises equivalent strain within a cross-section
220 through the center of the notch for an elongation of 0.6 and 0.7 mm, respectively. The strain

221 levels within the tomography specimens (Figure 3b-d) range between [0.3-0.45] and [0.4-0.6]
222 for the elongation of 0.6 mm and 0.7 mm, respectively.

223

224 **3.4. In situ X-Ray synchrotron holotomography heating**

225

226 The in situ 3D X-Ray nano-imaging tests were performed at the European Synchrotron
227 Radiation Facility (ESRF, Grenoble, France) on beamline ID16B using holotomography with
228 a voxel size of 35 nm and a dedicated high temperature furnace [27–29]. All 3D X-Ray nano-
229 imaging specimens were prepared according to the schematic in Figure 2c. The specimens were
230 thus taken from interrupted in situ SEM tensile tests at 0.6 mm and 0.7 mm of global elongation
231 (corresponding to a strain level of about 0.35 and 0.5 respectively, see section 3.3). They were
232 extracted next to the notch, i.e. in the region experiencing the largest strain and thus presenting
233 the highest level of damage (Figure 2c). The samples were then thinned manually to 200 μm
234 and cut by a micro-cutting machine. The specimens were mounted on a dedicated specimen
235 support (Figure 2c) to fit into the furnace available at the beamline [27]. The furnace can be
236 easily mounted and removed over the specimens to heat them up to 200, 300 and 400 $^{\circ}\text{C}$
237 between holotomography scans without moving the specimens. The nano-imaging were
238 acquired using a conic pink beam ($\Delta E/E=10^{-2}$) with an energy of 17.5 keV. While the specimen
239 rotated over 360° , 2D phase contrast images of the specimen (field of view: $90 \times 76 \mu\text{m}^2$ – pixel
240 size: 35 nm) were recorded using a CMOS camera. For each tomographic scan, 3009
241 projections were acquired with an exposure time of 200 ms per step.

242 For selected scanning steps, cavities were distinguished from the Al matrix by
243 segmentation and their geometrical characteristics were recorded. A tracking algorithm (in-
244 house built toolbox in MATLAB), relying on a graph-based data association approach, has been
245 modified and used to follow the cavities from one scanning step to the next (see Supplementary
246 material 5 for details of the procedure) [30,31]. Only the cavities with initial size above 0.1 μm
247 (i.e. with a diameter of at least 3 voxels) were used for the tracking procedure in order to avoid
248 counting any noise of the reconstructed images. The results of the tracking algorithm allow to
249 perform a statistical analysis of void healing, i.e. voids which have completely disappeared.

250 Supplementary material 2 provides a detailed list of all samples with the elongation used
251 before 3D X-Ray nano-imaging, the healing temperatures and times. Reference samples
252 without adding the Mg strip were also manufactured to assess the influence of magnesium
253 addition on the healing potential. The results of these additional specimens are provided in
254 Supplementary material 4.

255

256 **3.5. In situ TEM heating**

257

258 TEM was used for in situ heating also using the FEI Osiris TEM operated at 200kV. The TEM
259 specimens were also prepared from interrupted in situ SEM tensile test at a global elongation
260 of 0.6 mm by analogy with the specimens for 3D X-Ray nano-imaging (Figure 2c), then also
261 thinned using ion-milling. A Gatan 652 double-tilt heating holder was used for the in situ TEM
262 heating experiments. To assess the healing mechanism, the optimum temperature of 400 °C
263 (see section 4.3) was used with heating interruption for observation. The heating time from
264 room temperature (RT) to 400 °C was less than 1 min. All images were taken in HAADF-
265 STEM mode to facilitate the observation of the particles and cracks.

266

267 **3.6. Micro-hardness and uniaxial tensile test**

268

269 Vickers micro-hardness testing was performed along the FSP nugget zone with a EMCO-test
270 DuraScan G5 indenter under 0.3 kg loading (HV0.3). Uniaxial tensile tests were performed on
271 a screw-driven universal machine under displacement control with 0.5 mm/min velocity. Flat
272 samples, with a cross-section of 2x6 mm², were machined along the FSP direction
273 (Supplementary material 1 and 7). The initial gauge length was equal to 22 mm. The true
274 fracture stress (defined as $\sigma_f = F_f/A_f$) and the true fracture strain (defined as $\epsilon_f = \ln(A_0/A_f)$) were
275 computed from the last force value F_f recorded before fracture, and from the initial and fractured
276 section area, A_0 and A_f , respectively. In order to identify the work of fracture (W_f), the area
277 under true stress-strain curves was calculated. The samples Al-0.5Mg₂Si-HHT were strained to
278 10, 15, 18 and 20% (i.e. UTS reached) of global elongation before the healing heat treatment
279 (HHT) was applied. The heat treatment was performed at 400 °C using Heraeus heating oven
280 by the placement of flat samples in contact with the heating plate and subsequent cooling in air.

281

282 **4. Results and discussion**

283

284 **4.1. Initial and damaged microstructure characterization**

285

286 After FSP with an embedded Mg strip, inductively coupled plasma (ICP) analysis shows
287 that the overall Mg content was increased by 3% (from 0.4 to 3.4 wt.%) (Supplementary
288 material 1, Table S1). Figure 4a-b show that the new alloy consists of an Al matrix rich in Mg,

289 containing about 0.5% surface fraction of Mg₂Si particles (in dark grey) and brittle Fe-rich
290 intermetallics (in white), which are always present in industrial aluminum alloys and are source
291 of damage as was shown by Hannard et al. [22]. Supplementary material 1 provides a
292 quantitative characterization of these Mg₂Si particles.

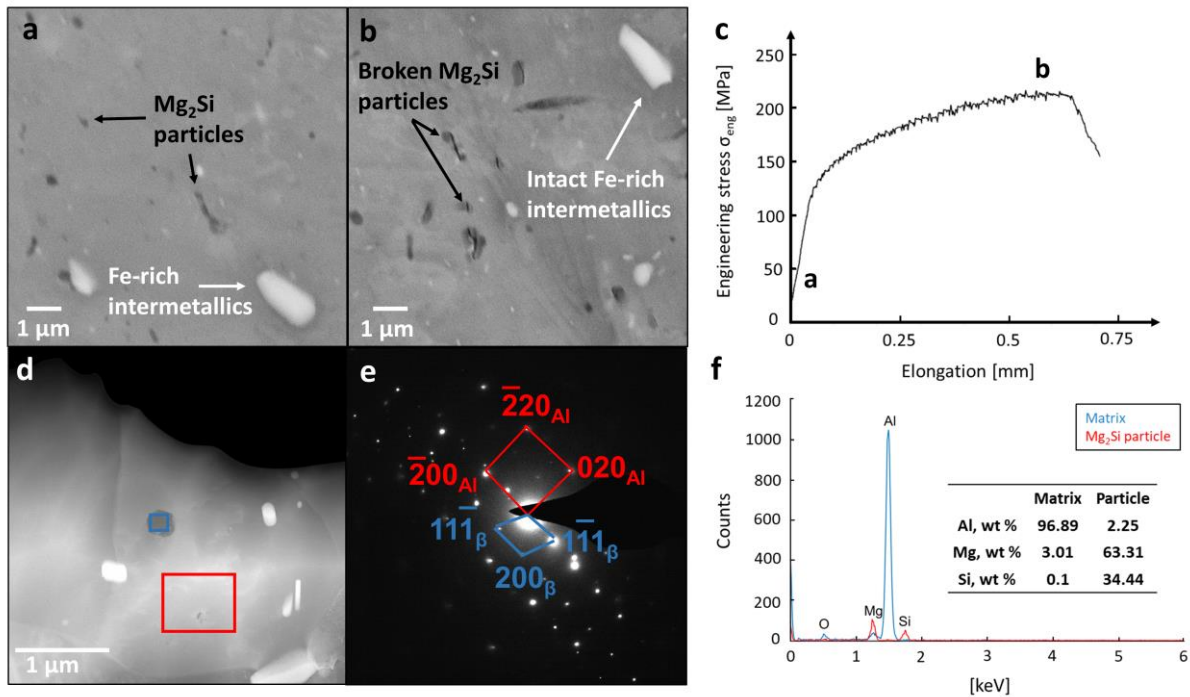
293 Homogeneously distributed 300 nm size Mg₂Si particles (Figure 4a) are formed in situ,
294 modifying the microstructure of Al6063 alloy and providing hardening effect. Selected area
295 electron diffraction pattern (SAED) in Figure 4e confirms that this phase is Mg₂Si. The hardness
296 of the nugget zone is increased from 52.36±0.94 for Al6063-FSP to 76.31±1.3 HV0.3 (see
297 Supplementary material 1, Figure S2 for full hardness map).

298 Fallah et al. [32] have shown that Mg enrichment in the matrix favors an early stage
299 Mg-Si clusters nucleation, stabilization and growth. These early stage clusters can easily be
300 transformed to an equilibrium Mg₂Si phase [33]. Figure 4d-f shows that the Si content is almost
301 entirely used for Mg₂Si precipitation (Figure 4d-f), while 3 wt.% Mg remains available in the
302 matrix (Figure 4f) for further healing. These results of the phases compositions correspond well
303 to the ones obtained by Thermo-Calc simulation for the same composition identified by ICP
304 analysis (Supplementary material 1, Table S2) at the expected FSP temperature of 490 ° C (≈
305 0.8 T_m). This means that the cooling rate after FSP was high enough to form a supersaturated
306 solid solution rich in Mg.

307 Both Mg₂Si particles and Mg enrichment of the Al matrix are important for the PDR
308 strategy: the Mg₂Si precipitates serve as damage sites and therefore generate Programmed
309 Damage, while the high diffusion rate of Mg in the Al matrix are expected to speed up void
310 healing (i.e. Repair) [10].

311 Figure 4b shows that damage initiates on Mg₂Si particles by their fracture or debonding
312 from the matrix only after significant tensile deformation during in situ SEM tensile testing
313 (Figure 4c), similar to Shen et al [34]. Fe-rich intermetallics remain generally intact until final
314 fracture, enabling large deformation range for healing before catastrophic failure, i.e. void
315 nucleation on brittle Fe-rich intermetallics in the matrix is effectively replaced by the
316 programmed damage at damage localization particles (for a proof with in-situ SEM tensile tests
317 see Supplementary material 3).

318



319
 320 **Figure 4.** Microstructure and damage evolution in Al6063-0.5Mg₂Si alloy. (a) Al6063-0.5Mg₂Si microstructure:
 321 in dark grey – Mg₂Si particles; in white – Fe-rich intermetallics; (b) damage nucleated on Mg₂Si particles at 0.6
 322 mm of global elongation; (c) tensile curve obtained during in situ scanning electron microscopy tensile test
 323 indicating the elongations corresponding to (a) and (b); (d) HAADF-STEM (high-angle annular dark-field
 324 scanning transmission electron microscopy) micrograph; (e) SAED (Selected Area Electron Diffraction) pattern
 325 obtained on a particle and the surrounding matrix; (f) EDX (Energy Dispersive X-Ray Analysis) analysis of a
 326 particle (blue box) and surrounding matrix (red box) indicated in (d). Both SAED and EDX confirm that these
 327 particles are Mg₂Si.

328
 329 This new alloy indeed presents novel microstructural features compared to previous
 330 solid-state SH metallic systems:

331 (i) small (below 1 μm) homogeneously distributed Mg₂Si particles are controlled
 332 damage sites limiting initial damage size;

333 (ii) enrichment of the Al matrix in Mg atoms speeds up solid-state diffusion at
 334 temperatures below homogenization while Al can also serve as healing agent [10];

335 (iii) since the matrix serves as a healing agent reservoir, the delivery of healing agents
 336 is continuous during applied HHT expectedly ensuring multiple healing cycles (Figure 1c) [35];

337 (iv) the “damage localization particles” present a strengthening effect as opposed to the
 338 underaged aluminum alloys (see introduction, PDP) [16,17].

339 In addition, a commercial 6063Al alloy is used as base material instead of alloys
 340 developed with specific compositions for SH purpose or high purity metallic systems [15,36].

341 Finally, FSP improves the ductility of the matrix material by up to 100% by microstructure
342 homogenization and refinement, and eliminates the need for any post-treatments [2,37,38].

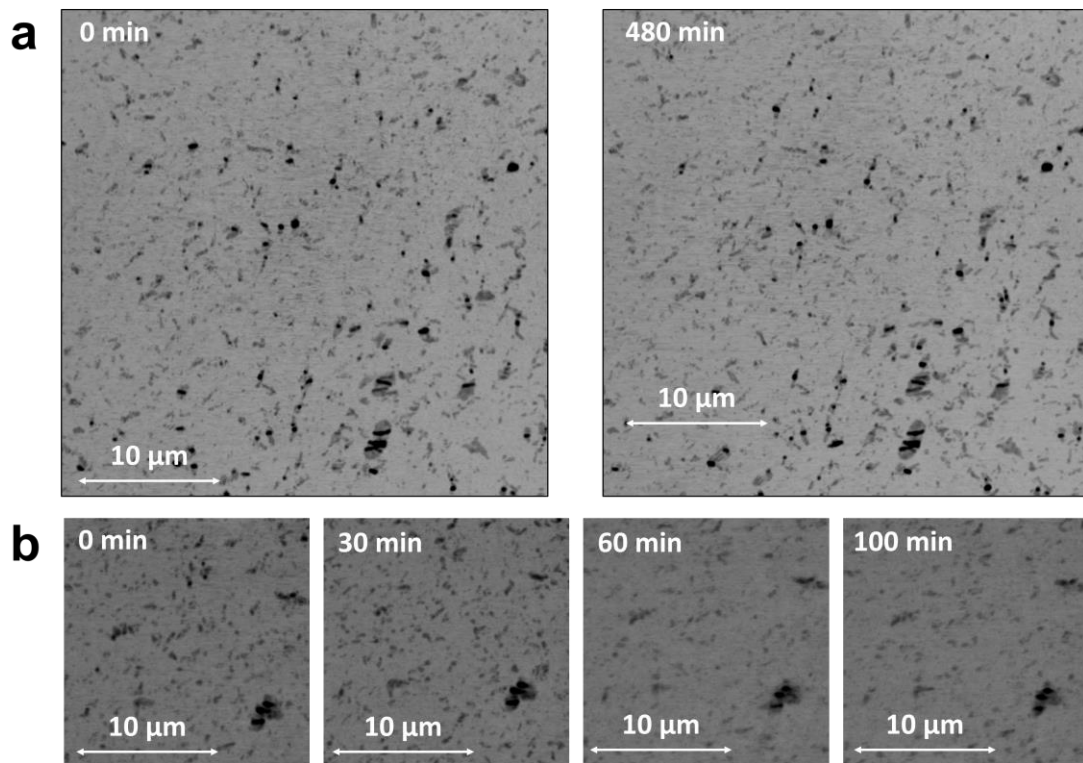
343

344 4.3. Selection of the healing temperature

345

346 3D X-ray nano-imaging was performed at the ESRF (see Supplementary material 2 for
347 sample full list). Three temperatures were selected to investigate the healing efficiency: 200,
348 300, and 400 °C, which correspond to values $T/T_m = 0.54, 0.65$ and 0.76 , with the melting
349 temperature of Al 6063 alloy taken as 610 °C or 883 K. These values are expected to be
350 sufficient to activate fast diffusing atoms. Figure 5 presents microstructural evolutions for
351 healing at 200 °C and 300 °C.

352



353

354 **Figure 5.** Minimum Intensity Projections (MinIP) of 50 slices of volumes obtained before and after heat treatment
355 (a) up to 8 hours at 200 °C and (b) and up to 100 minutes at 300 °C using X-ray holotomography. These specimens
356 correspond respectively to Specimen 4 and 5 of Supplementary material 2.

357 It is observed that for the 200 °C heating temperature (Figure 5a), even 8 hours are not
358 sufficient to cause healing and most voids remain unaffected. Similarly, 100 minutes at 300 °C
359 are not sufficient to show significant healing (Figure 5b). Although the healing of the voids is
360 more prominent at 300 °C, it still cannot be considered sufficient in comparison with a healing

361 temperature of 400 °C (Figure 6). Thus, in what follows, 400 °C will be selected as healing
362 temperature and the relevant temperature range of PDR is placed in Figure 1(b,c).

363

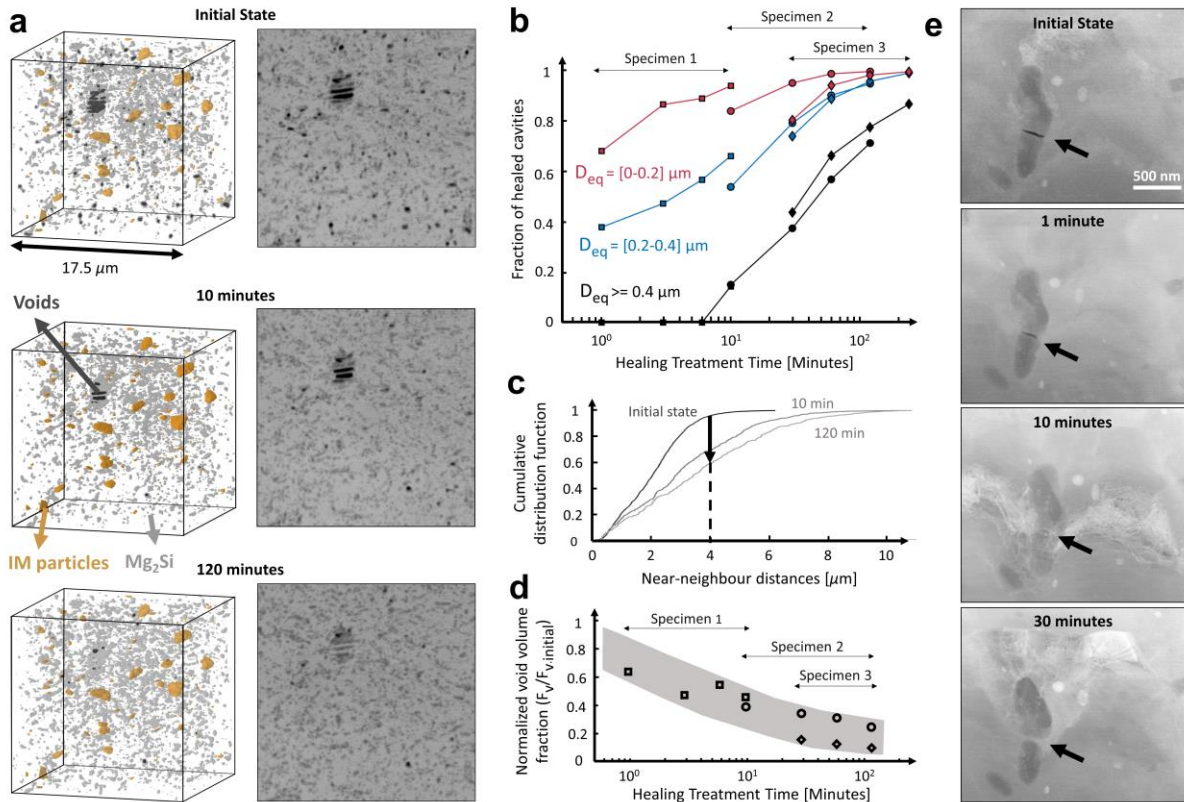
364 **4.2. Statistical validation of healing ability**

365

366 Correlative characterization over time was used to analyze healing ability [39]. Figure
367 6a shows the disappearance and progressive filling of larger voids observed during in situ HHT
368 coupled to 3D X-ray nano-imaging performed at the selected temperature of 400 °C. Figure 6b
369 shows the results of the tracking algorithm used to follow the progressive filling of each
370 individual void from one 3D scan to the next. A clear size effect is observed: the smallest
371 cavities (below 200 nm) have a healing efficiency of approximately 90% after 10 minutes, while
372 the largest cavities (larger than 400 nm) present a much lower healing efficiency (20%). Further
373 heating shows continuous healing of voids regardless of their size or deformation level at which
374 HHT is performed. After 2 hours, approximately 85% of all nucleated voids are completely
375 filled and the biggest healed void is about 2 μm in length (Figure 6a).

376 Figure 6c shows the cumulative distribution function of the near-neighbor distance
377 (NND) of each void just after damage (initial state) and after various HHT durations. It shows
378 that a lot of voids have at least one neighbor in very close proximity in the initial state (i.e.
379 small NND), while voids become distant from each other after HHT (i.e. larger NND). For
380 example, while all voids have a NND below 4 μm in the initial state, only 60% of voids have a
381 neighbor located at less than 4 μm after 10 minutes of HHT (Figure 6c). Healing postpones thus
382 failure as only closely spaced voids are likely to merge to form micro-cracks.[22] Figure 6d
383 shows that the void volume fraction is already significantly decreased after 10 minutes of HHT.
384 Clearly 10 minutes HHT is thus sufficient to significantly decrease both the number of voids
385 close to each other and the volume fraction of voids.

386



387
 388 **Figure 6.** Healing evolution with time at 400 °C. (a) 3D volumes and corresponding Minimum Intensity
 389 Projections (MinIP) in the initial state, after 10 minutes and after 2 hours at 400°C; (voids are in black,
 390 intermetallic particles in yellow and Mg₂Si particles in grey). (b) Evolution of the number of healed cavities with
 391 healing time for different size classes: Specimens 1 and 2 correspond to 0.6 mm of global elongation; Specimen 3
 392 corresponds to 0.7 mm of global elongation (see Supplementary material 2 for details on each specimen). (c)
 393 Cumulative distribution function (CDF) of the near-neighbour distances between voids as a function of the heating
 394 time. (d) Evolution of the void volume fraction (F_v), normalised by the value in the initial state ($F_{v,init}$). (e) HAADF-
 395 STEM images showing healing evolution with time. The black arrows indicate the position of the crack.

396
 397 **4.3. Healing mechanism**

398
 399 Figure 6e shows results of in situ heating in the transmission electron microscope at
 400 400°C with a typical example of healing mechanism (more results are provided in
 401 Supplementary material 6). The healing shown in Figure 6 can be interpreted by analogy with
 402 metal sintering, where the driving force of initial porosity closure is the decrease in interfacial
 403 energy, achieved by a reduction in free surface area per unit volume [5,40]. Thermal activation
 404 is required to trigger diffusion and start voids filling (by analogy with densification during
 405 sintering). At elevated temperature, diffusion is enhanced and oriented following the chemical
 406 potential gradient issued from concentration gradient: atoms will diffuse from areas presenting
 407 high concentration towards areas with lower concentration.

408 By analogy with sintering, a sharp crack tip can be considered as a void with a very low
409 dihedral angle. Low dihedral angles promote densification, favoring crack filling (Figure 6e)
410 [41]. The developed Al-0.5Mg₂Si alloy facilitates this process in three ways, which expectedly
411 work in parallel.

412 (i) FSP generates high density of defects as vacancies, dislocations and grain
413 boundaries, as well as a very fine distribution of Mg₂Si particles mainly forming at grain
414 boundaries (Supplementary material 6) [26]. Broken particles are thus connected to these
415 diffusion “shortcuts” and grain boundary diffusion of Al and Mg atoms can easily be activated
416 [24].

417 (ii) The region in front of the crack tip presents high stress concentration and higher
418 dislocation density providing a favorable path for pipe diffusion [24].

419 (iii) While an increase of Mg atoms concentration was not detected in the area of a
420 healed crack (Supplementary material 6, Figure S10), the supersaturated solid solution of Mg
421 atoms within the Al matrix (about 3%, Figure 4d,f) is expected to play a significant role in
422 healing kinetics and also contribute to the two factors discussed above [10]. Mg atoms have a
423 higher diffusion rate in the Al matrix than Al self-diffusion [10]. The solubility of Mg in the Al
424 matrix is below 1% at room temperature and Mg should remain as super-saturated atoms or
425 gather in Al-Mg rich GP zones [42,43]. The 400 °C HHT increases the solubility of Mg in Al
426 to about 13% leading to a release of all trapped Mg atoms from the clusters to the matrix for
427 diffusion and healing [44]. Mg atoms are neighboring and accompanying vacancies and
428 dislocations because of steric effects [45,46]. Heating will activate the migration of a flux of
429 defects towards grain boundaries acting as a sink [45,47]. Thus, Mg atoms trapped at these
430 defects will diffuse from the matrix to the grain boundary where they can further travel along
431 the grain boundary towards the crack (Figure 1a). Now the question is how can vacancies
432 annihilate? By analogy with the final stage of sintering, grain boundaries can act as healing
433 atoms source as well as vacancies sink [40,48].

434 In order to confirm the unique healing behavior of the proposed healable alloy and
435 indirectly verify the importance of Mg enrichment, the same commercial alloy Al6063 was
436 processed under the same condition but without Mg strip addition. In that case, the same healing
437 phenomenon was not observed (Figure S5 of Supplementary material 4).

438
439
440
441

442 **4.4. Effect of healing treatment on tensile properties**

443

444 To evaluate the effect of healing efficiency on mechanical properties, another kind of
445 tensile tests was performed (Supplementary material 7) on three Al-0.5Mg₂Si alloys (Figure 7a,
446 Table 1):

447 (1) as-FSPed (called Al-0.5Mg₂Si);

448 (2) non-damaged but heat treated at 400 °C for 10 min (called Al-0.5Mg₂Si-HT);

449 (3) damaged by loading to deformation levels up to 20% (details in Supplementary
450 material 7), heat treated then loaded until final failure (called Al-0.5Mg₂Si-HHT).

451

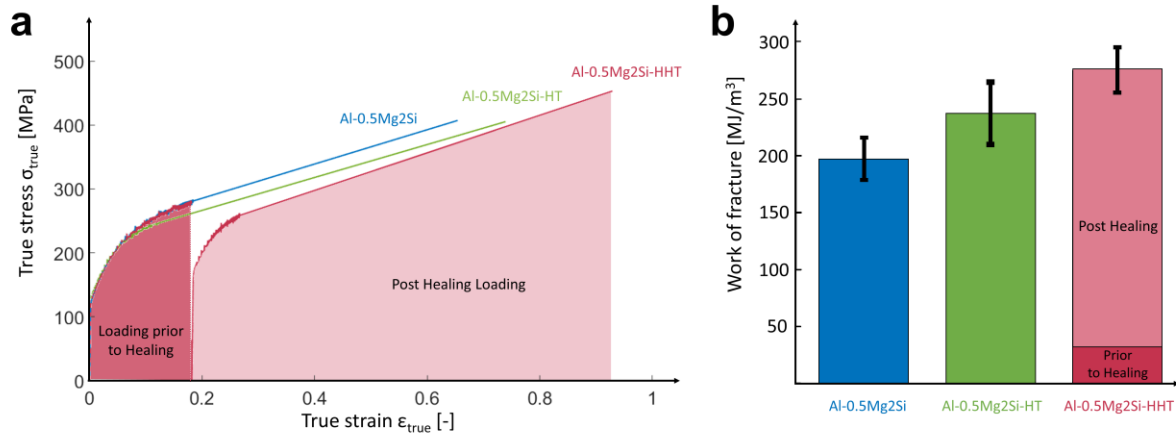
452 Heat treating the undamaged alloy improves the fracture strain ϵ_f from 0.65 ± 0.06 (Al-
453 0.5Mg₂Si) to 0.76 ± 0.05 (Al-0.5Mg₂Si-HT) without significantly affecting yield strength (σ_y)
454 (Figure 7a, Table 1) likely due to static recovery of the FSPed microstructure [49].

455 Al-0.5Mg₂Si-HHT was deformed up to strain close to the onset of plastic localization.
456 At this stage, particles are fractured (Figure 4b), and if no healing is applied before further
457 deformation, voids will grow, coalesce into macrocracks leading to catastrophic failure.
458 However, damage is significantly decreased by applying HHT. Al-0.5Mg₂Si-HHT presents a
459 similar fracture strain to Al-0.5Mg₂Si-HT: 0.74 ± 0.03 (or 0.90 ± 0.07 taking into account the
460 deformation applied before healing).

461 The work of fracture (W_f) quantifies the amount of energy that the material can absorb
462 before failure, evaluated from the area under the true stress-strain curves (Figure 7a), and is
463 used as an indicator of fracture toughness [38,50]. Figure 7b shows that healing recovers the
464 work of fracture of the damaged but post-healed sample (considering only the “Post Healing”
465 cycle) to a level similar to the Al-0.5Mg₂Si-HT sound sample. In addition, the total work of
466 fracture of the healed Al-0.5Mg₂Si-HHT sample (including both loading “Prior to Healing” and
467 “Post Healing” cycles) is 40% above that of Al-0.5Mg₂Si (Figure 7b, Supplementary material
468 7, Table S5).

469 An overall analysis of the curve indicated as “Post Healing Loading” in Figure 7a shows
470 that the material after HHT does not present any yield stress, ultimate tensile stress, fracture
471 strain nor work of fracture loses compared to Al-0.5Mg₂Si-HT and in this perspective behaves
472 like undamaged material even though it underwent the “Loading prior to Healing” cycle
473 generating damage.

474



475

476 **Figure 7.** Mechanical behavior of Al-0.5Mg₂Si samples. (a) Typical true stress-strain curves of the Al-0.5Mg₂Si
 477 samples; (b) corresponding work of fracture.

478

479 **Table 1.** Mean values for tensile properties of the composite samples before and after the healing heat treatments

| | E ^{a)} [GPa] | σ_y [MPa] | $\sigma_y^{b)}$ [MPa] | $\sigma_{Failure}^{c)}$ [MPa] | ϵ_f | $W_f^{b)}$ [MJ/m ³] | W_f [MJ/m ³] |
|------------------------------|--------------------------|---------------------|--------------------------|----------------------------------|--------------|------------------------------------|-------------------------------|
| Al-0.5Mg ₂ Si | 69.3±1.2 | 124.8±3.1 | | 394.73±10.7 | 0.65±0.1 | | 196.3±15.3 |
| Al-0.5Mg ₂ Si-HT | 67.1±0.8 | 131.5±3.0 | | 416.90±29.6 | 0.76±0.00 | | 236.6±23.5 |
| Al-0.5Mg ₂ Si-HHT | 67.0±3.8 | 125.7±4.2 | 175.6±9.3 | 428.9±32.8 | 0.74±0.03 | 242.5±12.1 | 273.7±16.8 |

^{a)} E – Young modulus; ^{b)} data for Post Healing Loading curve; ^{c)} $\sigma_{Failure}$ – Strength at failure

480

481 One should note that recovery, recrystallization and in general heat treatment softening
 482 mechanisms also play a role on the tensile behavior after the HHT. Now, compare samples Al-
 483 0.5Mg₂Si-HHT and Al-0.5Mg₂Si-HT (Figure 7b). The 16% improved W_f with the same heat
 484 treatment (including both loading “Prior to Healing” and “Post Healing” cycles), i.e. expectedly
 485 leading to a similar softening, brings the conclusion that damage healing contributes to W_f of
 486 the healed sample (Al-0.5Mg₂Si-HHT). Indeed, voids (i.e. small cracks) closure causes a
 487 reduction in NND (Figure 6c). For neighboring damage to coalesce, regions of elevated strain
 488 (the regions in front of the crack tips) should overlap. The HHT increases the distance between
 489 voids and thus postpones void coalescence.

490

491 5. Conclusion and outlook

492

493 This work presents a new precipitation-based healing strategy for metals. A proof of
 494 concept using commercial Al alloy shows that one healing cycle fully recovers mechanical
 495 properties and overall improves work of fracture by 40% compared to the initial state of the
 496 material. The proposed Programmed Damage and Repair (PDR) strategy overcomes many

497 reported limitations for self-healing (or healable) Al-based alloys particularly taking a step
498 forward from nanoscale damage healing to a few microns scale. Further development of PDR
499 strategy achieving full healing is expected to lead to multi-cycle healable alloy. Moreover, as
500 FSP can be applied locally or like a surface treatment in commercial Al alloys, these new
501 healable alloys could enhance local areas of stress concentrations, granting prolonged service
502 life to structures.

503 Although not investigated yet, we anticipate that our concept could expand to other
504 alloys with a precipitation phenomenon (e.g., 7xxx Al alloys, Mg alloys). As a result, the PDR
505 strategy has great potential to impact the classical paradigm in metallic materials design, where
506 only damage delay and prevention are considered as optimization routes. In addition, the
507 proposed strategy can be adopted by other processes where two conditions meet: possibility to
508 modify chemical composition in order to obtain damage localization particles and
509 supersaturated solid solution; and possibility to control processing conditions so fine
510 microstructures presenting diffusion shortcuts can be produced and well-controlled, e.g.,
511 additive manufacturing.

512

513 **Acknowledgements**

514 This work was supported by the European Research Council for a starting grant [grant
515 agreement - 716678], the Belgian National Fund for Scientific Research – FNRS, Belgium
516 [Grant CDR – J.0113.20, FRIA grant - 35484217] and the ESRF for provision of radiation
517 facilities [proposal MA-4353]. F.H. acknowledges the Belgian National Fund for Scientific
518 Research (FNRS) for his postdoctoral fellowship at UCLouvain. H. Idrissi is mandated by the
519 Belgian National Fund for Scientific Research (FSR-FNRS).

520

521

522 **References**

- 523 [1] I. Polmear, D. StJohn, J.-F. Nie, M. Qian, *Light Alloys: Metallurgy of the Light*
524 *Metals*, 5th ed., Butterworth-Heinemann, 2017. doi:10.1016/b978-0-08-099431-
525 4.00010-5.
- 526 [2] F. Hannard, S. Castin, E. Maire, R. Mokso, T. Pardoën, A. Simar, Ductilization of
527 aluminium alloy 6056 by friction stir processing, *Acta Mater.* 130 (2017) 121–136.
528 doi:10.1016/j.actamat.2017.01.047.
- 529 [3] N. Kamp, I. Sinclair, M.J. Starink, Toughness-strength relations in the overaged 7449
530 Al-based alloy, *Metall. Mater. Trans. A Phys. Metall. Mater. Sci.* 33 (2002) 1125–

- 531 1136. doi:10.1007/s11661-002-0214-2.
- 532 [4] L. Zhao, J.G. Santos Macías, L. Ding, H. Idrissi, A. Simar, Damage mechanisms in
533 selective laser melted AlSi10Mg under as built and different post-treatment conditions,
534 Mater. Sci. Eng. A. 764 (2019) 138210. doi:10.1016/j.msea.2019.138210.
- 535 [5] N. van Dijk, S. van der Zwaag, Self-Healing Phenomena in Metals, Adv. Mater.
536 Interfaces. 5 (2018) 1–13. doi:10.1002/admi.201800226.
- 537 [6] B. Grabowski, C.C. Tasan, Self-Healing Metals, in: M.D. Hager, S. van der Zwaag,
538 U.S. Schubert (Eds.), Self-Healing Mater., Springer International Publishing
539 Switzerland, 2016: pp. 387–408. doi:10.1007/12_2015_337.
- 540 [7] V. Srivastava, M. Gupta, Approach to self healing in Metal matrix Composites: A
541 review, Mater. Today Proc. 5 (2018) 19703–19713. doi:10.1016/j.matpr.2018.06.332.
- 542 [8] P.K. Nosonovsky, Michael, Rohatgi, Biomimetics in Materials Science, 1st ed.,
543 Springer-Verlag New York, 2012. doi:10.1007/978-1-4614-0926-7.
- 544 [9] S. Zhang, N. van Dijk, S. van der Zwaag, A Review of Self-healing Metals:
545 Fundamentals, Design Principles and Performance, Acta Metall. Sin. (English Lett. 33
546 (2020) 1167–1179. doi:10.1007/s40195-020-01102-3.
- 547 [10] M. Song, K. Du, S.P. Wen, Z.R. Nie, H.Q. Ye, In situ electron microscopy
548 investigation of void healing in an Al-Mg-Er alloy at a low temperature, Acta Mater.
549 69 (2014) 236–245. doi:10.1016/j.actamat.2014.02.004.
- 550 [11] H.J. Jeong, M.J. Kim, S.J. Choi, J.W. Park, H. Choi, V.T. Luu, S.T. Hong, H.N. Han,
551 Microstructure reset-based self-healing method using sub-second electric pulsing for
552 metallic materials, Appl. Mater. Today. 20 (2020) 100755.
553 doi:10.1016/j.apmt.2020.100755.
- 554 [12] X. Ren, Z. Wang, X. Fang, H. Song, J. Duan, The plastic flow model in the healing
555 process of internal microcracks in pre-deformed TC4 sheet by pulse current, Mater.
556 Des. 188 (2020) 108428. doi:10.1016/j.matdes.2019.108428.
- 557 [13] G. Siroky, E. Kraker, J. Rosc, D. Kieslinger, R. Brunner, S. Van Der Zwaag, E.
558 Kozeschnik, W. Ecker, Analysis of SN-BI solders: X-ray micro computed tomography
559 imaging and microstructure characterization in relation to properties and liquid phase
560 healing potential, Materials (Basel). 14 (2021) 1–22. doi:10.3390/ma14010153.
- 561 [14] M. Arsenko, J. Gheysen, F. Hannard, N. Nothomb, A. Simar, Self-Healing in Metal-
562 Based Systems, in: A. Kanellopoulos, J. Norambuena-Contreras (Eds.), Self-Healing
563 Constr. Mater., 1st ed., Springer Nature Switzerland AG, 2022: pp. 43–78.
564 doi:https://doi.org/10.1007/978-3-030-86880-2_3.

- 565 [15] H. Fang, N. Szymanski, C.D. Versteyleen, P. Cloetens, C. Kwakernaak, W.G. Sloof,
566 F.D. Tichelaar, S. Balachandran, M. Herbig, E. Brück, S. van der Zwaag, N.H. van
567 Dijk, Self healing of creep damage in iron-based alloys by supersaturated tungsten,
568 *Acta Mater.* 166 (2019) 531–542. doi:10.1016/j.actamat.2019.01.014.
- 569 [16] S. Hautakangas, H. Schut, N.H. van Dijk, P.E.J. Rivera Díaz del Castillo, S. van der
570 Zwaag, Self-healing of deformation damage in underaged Al-Cu-Mg alloys, *Scr.*
571 *Mater.* 58 (2008) 719–722. doi:10.1016/j.scriptamat.2007.11.039.
- 572 [17] M. Mahdavi Shahri, R.C. Alderliesten, S. van der Zwaag, H. Schut, Postponing Crack
573 Nucleation in 2024 Aluminium Alloy by Dynamic Precipitation from the
574 Supersaturated State, *Adv. Mater. Res.* 891–892 (2014) 1577–1584.
575 doi:10.4028/www.scientific.net/amr.891-892.1577.
- 576 [18] R.N. Lumley, A.J. Morton, I.J. Polmear, Enhanced creep performance in an Al-Cu-Mg-
577 Ag alloy through underageing, *Acta Mater.* 50 (2002) 3597–3608. doi:10.1016/S1359-
578 6454(02)00164-7.
- 579 [19] R. Djugum, R.N. Lumley, D.M. Viano, C.J. Davidson, Enhanced Fatigue Resistance in
580 a Commercial Al-Cu-Mg Alloy through Underageing, in: *2nd Int. Conf. Self Heal.*
581 *Mater.*, 2009: pp. 8–11.
- 582 [20] R. J. H. Wanhill, Fatigue Crack Initiation in Aerospace Aluminium Alloys ,
583 Components and Structures, in: *Proc. First Int. Conf. Self Heal. Mater.*, Springer, 2007:
584 pp. 1–19.
- 585 [21] N. Chawla, K.K. Chawla, *Metal Matrix Composites*, Second Edi, Springer-Verlag New
586 York, New York, 2013. doi:10.1007/978-1-4614-9548-2.
- 587 [22] F. Hannard, A. Simar, E. Maire, T. Pardoën, Quantitative assessment of the impact of
588 second phase particle arrangement on damage and fracture anisotropy, *Acta Mater.* 148
589 (2018) 456–466. doi:10.1016/j.actamat.2018.02.003.
- 590 [23] R. Lumley, Self Healing in Aluminium Alloys, in: S. van der Zwaag (Ed.), *Self-*
591 *Healing Mater. An Altern. Approach to 20 Centuries Mater. Sci.*, Springer, 2007: pp.
592 219–254. doi:10.1007/978-1-4020-6250-6_11.
- 593 [24] Z. Balogh, G. Schmitz, Diffusion in Metals and Alloys, in: *Phys. Metall. Fifth Ed.*,
594 Fifth Edit, Elsevier, 2014: pp. 387–559. doi:10.1016/B978-0-444-53770-6.00005-8.
- 595 [25] R. Bauri, D. Yadav, *Processing Metal Matrix Composite (MMC) by FSP*, Butterworth-
596 Heinemann, 2018. doi:10.1016/b978-0-12-813729-1.00003-6.
- 597 [26] A. Heidarzadeh, S. Mironov, R. Kaibyshev, G. Çam, A. Simar, A. Gerlich, F.
598 Khodabakhshi, A. Mostafaei, D.P. Field, J.D. Robson, A. Deschamps, P.J. Withers,

- 599 Friction stir welding/processing of metals and alloys: A comprehensive review on
600 microstructural evolution, *Prog. Mater. Sci.* 117 (2020) 100752.
601 doi:10.1016/j.pmatsci.2020.100752.
- 602 [27] J. Villanova, R. Daudin, P. Lhuissier, D. Jauffrès, S. Lou, C.L. Martin, S. Labouré, R.
603 Tucoulou, G. Martínez-Criado, L. Salvo, Fast in situ 3D nanoimaging: a new tool for
604 dynamic characterization in materials science, *Mater. Today*. 20 (2017) 354–359.
605 doi:10.1016/j.mattod.2017.06.001.
- 606 [28] P. Cloetens, W. Ludwig, J. Baruchel, D. Van Dyck, J. Van Landuyt, J.P. Guigay, M.
607 Schlenker, Holotomography: Quantitative phase tomography with micrometer
608 resolution using hard synchrotron radiation x rays, *Appl. Phys. Lett.* 75 (1999) 2912–
609 2914. doi:10.1063/1.125225.
- 610 [29] G. Martinez-Criado, J. Villanova, R. Tucoulou, D. Salomon, J.P. Suuronen, S.
611 Laboure, C. Guilloud, V. Valls, R. Barrett, E. Gagliardini, Y. Dabin, R. Baker, S.
612 Bohic, C. Cohen, J. Morse, ID16B: A hard X-ray nanoprobe beamline at the ESRF for
613 nano-analysis, *J. Synchrotron Radiat.* 23 (2016) 344–352.
614 doi:10.1107/S1600577515019839.
- 615 [30] F. Hannard, T. Pardoën, E. Maire, C. Le Bourlot, R. Mokso, A. Simar, Characterization
616 and micromechanical modelling of microstructural heterogeneity effects on ductile
617 fracture of 6xxx aluminium alloys, *Acta Mater.* 103 (2016) 558–572.
618 doi:10.1016/j.actamat.2015.10.008.
- 619 [31] L. Lecarme, E. Maire, A. Kumar, C. De Vleeschouwer, L. Jacques, A. Simar, T.
620 Pardoën, Heterogenous void growth revealed by in situ 3-D X-ray microtomography
621 using automatic cavity tracking, *Acta Mater.* 63 (2014) 130–139.
622 doi:10.1016/j.actamat.2013.10.014.
- 623 [32] V. Fallah, B. Langelier, N. Ofori-Opoku, B. Raeisinia, N. Provatas, S. Esmaili,
624 Cluster evolution mechanisms during aging in Al-Mg-Si alloys, *Acta Mater.* 103
625 (2016) 290–300. doi:10.1016/j.actamat.2015.09.027.
- 626 [33] G.A. Edwards, K. Stiller, G. Dunlop, APFIM investigation of fine-scale precipitation
627 in Aluminium Alloy 6061, *Appl. Surf. Sci.* 77 (1994) 219–225.
- 628 [34] Y. Shen, T.F. Morgeneyer, J. Garnier, L. Allais, L. Helfen, J. Crépin, Three-
629 dimensional quantitative in situ study of crack initiation and propagation in AA6061
630 aluminum alloy sheets via synchrotron laminography and finite-element simulations,
631 *Acta Mater.* 61 (2013) 2571–2582. doi:10.1016/j.actamat.2013.01.035.
- 632 [35] K.S. Toohey, N.R. Sottos, J.A. Lewis, J.S. Moore, S.R. White, Self-healing materials

- 633 with microvascular networks, *Nat. Mater.* 6 (2007) 581–585. doi:10.1038/nmat1934.
- 634 [36] J.T. Kim, H.J. Kim, S.H. Hong, H.J. Park, Y.S. Kim, Y.J. Hwang, Y.B. Jeong, J.Y.
635 Park, J.M. Park, B. Sarac, W.M. Wang, J. Eckert, K.B. Kim, Thermally-triggered Dual
636 In-situ Self-healing Metallic Materials, *Sci. Rep.* 8 (2018) 2–11. doi:10.1038/s41598-
637 018-19936-4.
- 638 [37] Z. Li, C. Li, Y. Liu, L. Yu, Q. Guo, H. Li, Effect of heat treatment on microstructure
639 and mechanical property of Al-10%Mg₂Si alloy, *J. Alloys Compd.* 663 (2016) 16–19.
640 doi:10.1016/j.jallcom.2015.12.128.
- 641 [38] R. Zamani, H. Mirzadeh, M. Emamy, Mechanical properties of a hot deformed Al-
642 Mg₂Si in-situ composite, *Mater. Sci. Eng. A.* 726 (2018) 10–17.
643 doi:10.1016/j.msea.2018.04.064.
- 644 [39] T.L. Burnett, P.J. Withers, Completing the picture through correlative characterization,
645 *Nat. Mater.* 18 (2019) 1041–1049. doi:10.1038/s41563-019-0402-8.
- 646 [40] S.H. Huo, M. Qian, G.B. Schaffer, E. Crossin, Aluminium powder metallurgy,
647 Woodhead Publishing Limited, 2010. doi:10.1533/9780857090256.3.655.
- 648 [41] R.M. German, P. Suri, S. Jin, Review : liquid phase sintering, *J. Mater. Sci.* 44 (2009)
649 1–39. doi:10.1007/s10853-008-3008-0.
- 650 [42] S. Nebti, D. Hamana, G. Cizeron, Calorimetric study of pre-precipitation and
651 precipitation in Al-Mg alloy, *Acta Metall. Mater.* 43 (1995) 3583–3588.
652 doi:10.1016/0956-7151(95)00023-O.
- 653 [43] M.J. Starink, A.M. Zahra, β' and β precipitation in an Al-Mg alloy studied by DSC and
654 TEM, *Acta Mater.* 46 (1998) 3381–3397. doi:10.1016/S1359-6454(98)00053-6.
- 655 [44] W. Wen, Y. Zhao, J.G. Morris, The effect of Mg precipitation on the mechanical
656 properties of 5xxx aluminum alloys, *Mater. Sci. Eng. A.* 392 (2005) 136–144.
657 doi:10.1016/j.msea.2004.09.059.
- 658 [45] R. Goswami, P.S. Pao, S.B. Qadri, R.L. Holtz, Severe plastic deformation induced
659 sensitization of cryo-milled nanocrystalline Al-7.5 Mg, *Metall. Mater. Trans. A Phys.*
660 *Metall. Mater. Sci.* 45 (2014) 2894–2898. doi:10.1007/s11661-014-2227-z.
- 661 [46] R.C. Picu, D. Zhang, Atomistic study of pipe diffusion in Al-Mg alloys, *Acta Mater.* 52
662 (2004) 161–171. doi:10.1016/j.actamat.2003.09.002.
- 663 [47] G. Yi, A.T. Derrick, Y. Zhu, M.L. Free, A Collector Plate Mechanism-Based Classical
664 Intergranular Precipitation Model for Al Alloys Sensitized at Different Temperatures,
665 *Metall. Mater. Trans. A Phys. Metall. Mater. Sci.* 46 (2015) 5393–5406.
666 doi:10.1007/s11661-015-3110-2.

- 667 [48] S.J.L. Kang, Y. Il Jung, Sintering kinetics at final stage sintering: Model calculation
668 and map construction, *Acta Mater.* 52 (2004) 4573–4578.
669 doi:10.1016/j.actamat.2004.06.015.
- 670 [49] K.J. Al-Fadhalah, A.I. Almazrouee, A.S. Aloraier, Microstructure and mechanical
671 properties of multi-pass friction stir processed aluminum alloy 6063, *Mater. Des.* 53
672 (2014) 550–560. doi:10.1016/j.matdes.2013.07.062.
- 673 [50] L. Choisez, L. Ding, M. Marteleur, H. Idrissi, T. Pardoën, P.J. Jacques, High
674 temperature rise dominated cracking mechanisms in ultra-ductile and tough titanium
675 alloy, *Nat. Commun.* 11 (2020) 1–8. doi:10.1038/s41467-020-15772-1.
- 676